



Electrolytes at interfaces: accessing the first nanometers using X-ray standing waves

Soumaya Ben-Jabrallah, Florent Malloggi, Luc Belloni, Luc Girard, Dmitri Novikov, Cristian Mocuta, Dominique Thiaudière, Jean Daillant

► To cite this version:

Soumaya Ben-Jabrallah, Florent Malloggi, Luc Belloni, Luc Girard, Dmitri Novikov, et al.. Electrolytes at interfaces: accessing the first nanometers using X-ray standing waves. *Physical Chemistry Chemical Physics*, 2016, 19, pp.167 - 174. 10.1039/c6cp06888j . cea-01422226

HAL Id: cea-01422226

<https://cea.hal.science/cea-01422226>

Submitted on 24 Dec 2016

HAL is a multi-disciplinary open access archive for the deposit and dissemination of scientific research documents, whether they are published or not. The documents may come from teaching and research institutions in France or abroad, or from public or private research centers.

L'archive ouverte pluridisciplinaire **HAL**, est destinée au dépôt et à la diffusion de documents scientifiques de niveau recherche, publiés ou non, émanant des établissements d'enseignement et de recherche français ou étrangers, des laboratoires publics ou privés.

Electrolytes at Interfaces: Accessing the First Nanometers Using X-ray Standing Waves

Soumaya ben Jabrallah,[†] Florent Malloggi,^{*,†} Luc Belloni,[†] Luc Girard,[‡] Dmitri Novikov,[¶] Cristian Mocuta,[§] Dominique Thiaudière,[§] and Jean Daillant[§]

[†]LIONS, NIMBE, CEA, CNRS, Université Paris-Saclay, CEA Saclay 91191 Gif sur Yvette Cedex

[‡]ICSM UMR 5257 - CEA / CNRS / UM / ENSCM, Site de Marcoule, Bâtiment 426 BP 17171 F-30207 Bagnols sur Cèze Cedex

[¶]Deutsches Elektronensynchrotron DESY, Notkestrasse 85, D-22607 Hamburg, Germany

[§]Synchrotron SOLEIL, L'Orme des Merisiers, Saint-Aubin, BP 48, F-91192 Gif-sur-Yvette Cedex, France

E-mail: florent.malloggi@cea.fr

Abstract

Ion-surface interactions are of high practical importance in a wide range of technological, environmental and biological problems. In particular, they ultimately control the electric double layer structure, hence the interaction between particles in aqueous solutions. Despite numerous achievements, progress in their understanding is still limited by the lack of experimental determination of the surface composition with appropriate resolution. Tackling this challenge, we have developed a method based on X-ray standing waves coupled to nanconfinement which allows the determination of ion concentrations at a solid-solution interface with a sub-nm resolution. We have investigated mixtures of KCl/CsCl and KCl/KI in 0.1mM to 10mM concentrations on silica surfaces and obtained quantitative information on the partition of ions between bulk and Stern layer as well as their distribution in the Stern layer. Regarding partition of potassium ions, our results are in agreement with a recent AFM study. We show that in a mixture of KCl and KI, chloride ions exhibit a higher surface propensity than iodide ions, having a higher concentration within the Stern layer and being on average closer to

the surface by \approx 1-2 Å, in contrast to the solution water interface. Confronting such data with molecular simulations will lead to a precise understanding of ionic distributions at aqueous interfaces.

Introduction

The interfacial behavior of ions is of key importance in a number of phenomena and processes ranging from biological systems to micro- and nanofluidics. Ion-surface interactions are important both in a direct way, e.g. in sorption or ion exchange related effects, or indirectly because modifying the effective surface charge they will affect the structure of the electric double layer, hence the interaction between charged particles in aqueous solutions.¹ In this context, particularly interesting are the so-called “specific effects”, referring to phenomena where ions of the same valency have a different effect.²⁻⁴ These effects resulting from a subtle balance between polarisability, hydration and interfacial water structure usually follow “Hofmeister series” ($\text{SCN}^- > \text{ClO}_4^- \approx \text{I}^- > \text{Br}^- > \text{Cl}^- > \text{F}^-$ for anions) in direct or reverse order.⁴⁻⁶ They have a major effect on as diverse phe-

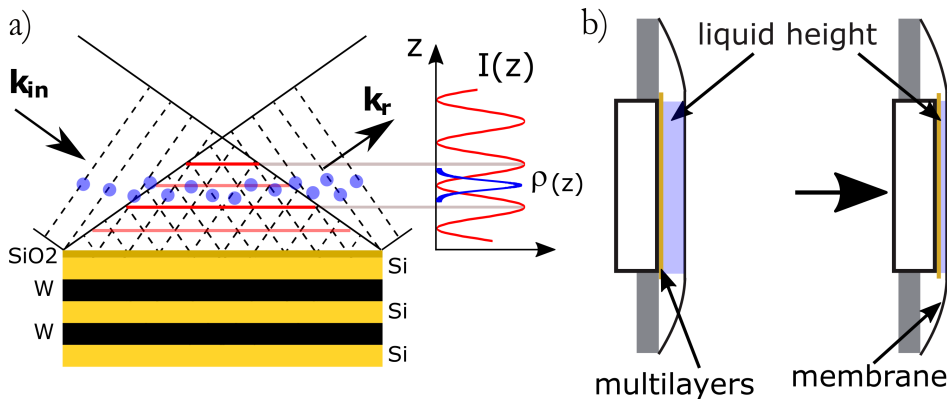


Figure 1: (a) Schematics of the standing wave experiment. Incident (wave vector \mathbf{k}_{in}) and reflected (wave vector \mathbf{k}_r) X-ray waves interfere to create a standing wave field perpendicular to the interface. The species (sketched by blue dots) present in the XSW field are excited and emit secondary fluorescence photons for absorption edges below the incident beam energy. (b) Schematics of the experimental cell. The liquid layer is confined between the multilayer and a flexible X-ray transparent membrane.

nomena as colloidal stability,² protein stability³ or the surface tension of electrolytes.⁷ In environmental sciences, the interaction between ions, humics and minerals influences the mobility and availability of pollutants.⁸ The interfacial behavior of ions is also of key importance in micro- and nanofluidics.⁹ Phenomena occurring within the diffuse Gouy-Chapman layer indeed become dominant in determining flow properties as channel size, Debye length and slip length become on the same order of magnitude, leading to unusual phenomena.¹⁰ For example, with charged walls, channels can be filled with a unipolar solution of counter-ions, suggesting that the type and concentration of ions can be controlled by the surface charge density of the channel wall.^{11,12} In addition, "specific effects" could allow for even finer control over the ion type as specific adsorption will eventually determine the double layer structure.¹³

Determining the interfacial distribution of ions with sufficient accuracy is, however, a challenge. Indeed, the ionic concentration deviates from the bulk concentration only in the Stern layer and diffuse Gouy-Chapman layer: from 1nm to 100nm depending on the solution concentration. Several surface sensitive techniques like photoemission,¹⁴⁻¹⁷ sum-frequency generation (SFG), second-harmonic generation (SHG),^{18,19} X-ray fluorescence⁷ or X-ray re-

flectivity^{20,21} have been used. More recently Atomic Force Microscopy has also been used to directly probe the electrical double layer.²²⁻²⁴ However, SFG and SHG have surface sensitivity but are not directly sensitive to ions and lack depth resolution, X-ray reflectivity or neutron reflectivity have no direct element sensitivity. Though photoemission has recently been extended to determine surface potential at the colloid/electrolyte interface,¹⁶ it has no direct sensitivity to the ion distribution. In this study, we used the X-ray standing waves (XSW) technique which has the advantage of having both element and depth sensitivity to probe the first nanometers at the solid surface. The technique first developed to locate atoms in crystals or adsorbed at crystal surfaces²⁵ has also been applied to soft condensed matter.²⁶ It has in particular been used to investigate the adsorption of heavy ions on crystal surfaces from solutions.^{27,28} We show here that the method can be extended to light ions (down to chlorine or sulfur) on surfaces like silica which are of very broad interest in colloidal science.

Experimental

The x-ray standing wave technique.

The X-ray standing waves (XSW) technique is based upon creating an electromagnetic standing wave field by interference between incident and Bragg reflected X-rays (Fig 1a).²⁹ The standing wave phase depends on the deviation from the exact Bragg angle and can be varied in a controlled way, thus moving the X-ray field nodes in a range spanning half of the diffraction plane spacing. The variation of secondary fluorescence signal coming from the atoms, that get excited by this XSW field, can be then used to locate the atom positions with (sub)Angstrom resolution. The method allows one to simultaneously investigate positions of different atoms, monitoring their specific emission lines. The standing waves are present where the incident and diffracted waves overlap, which includes the solid/liquid interface and the bulk solution above. A specific XSW variant especially suited for investigation of liquid/solid interfaces employs XSW generators, based on artificially grown multilayer structures (ML). Another advantage of this approach is the possibility to tune the resolution by changing the diffracting plane spacing as well as the large choice of ML materials. In particular it would be possible to apply an external bias by embedding a conducting layer in the ML. The ML-generated XSW were used for instance for investigation of Zn²⁺ distribution above a charged lipid layer²⁷ and in studies of electrochemical deposition of iodine on Pt.³⁰

In order to calculate the fluorescence intensity, the sample is divided in as many layers j as necessary to describe the elemental distribution. We choose the layers to be thin enough for the local density of element k in layer j $\rho_{k,j}(z)$ to be constant. The fluorescence intensity for element k at grazing angle of incidence θ is then given by:

$$I_k(\theta) = B_k \sum_{j=0}^s \int_{h_{j+1}}^{h_j} \rho_{k,j}(z) T_{k,j}(z) |E_j(z)|^2 dz, \quad (1)$$

where the constant B_k depends on the fluores-

cence yield, detection efficiency and geometrical factors. $E_j(z)$ is the electric field in layer j which is calculated in each layer using the matrix method.³¹ $T_{k,j}(z)$ is the transmission of the fluorescence intensity emitted by element k from layer j to the detector. As we are looking for nanometric layers close to the substrate, $T_{k,j}(z)$ is in fact independent of j . With this approximation,

$$I_k(\theta) = B_k T_k \sum_j \int_{h_{j+1}}^{h_j} |E_j(z)|^2 dz. \quad (2)$$

Writing for a plane wave

$$E_j(x, z) = (A_j^+ e^{ik_{z,j} z} + A_j^- e^{-ik_{z,j} z}) e^{+i(\omega t - k_{x,j} x)}, \quad (3)$$

where the A_j^\pm coefficients are determined using the matrix method following³¹ and integrating over layer j , one simply has:

$$\begin{aligned} \int_{h_{j+1}}^{h_j} |E_j(z)|^2 dz &= \frac{|A_j^+|^2}{2k_z^i} [1 - \exp(-2k_z^i \delta h)] \\ &+ \frac{|A_j^-|^2}{2k_z^i} [\exp(2k_z^i \delta h) - 1] \\ &+ \frac{|A_j^{+*} A_j^-|}{2ik_z^r} [1 - \exp(-2ik_z^r \delta h)] \\ &+ \frac{|A_j^+ A_j^{-*}|}{2ik_z^r} [\exp(2ik_z^r \delta h) - 1] \end{aligned} \quad (4)$$

with $\delta h = h_j - h_{j+1}$.

Though this method is accurate, it does not allow one to develop an intuition of the expected shape of the standing wave curve. For a monolayer located at z , one would have

$$I(\theta, z) = 1 + R(\theta) + 2\sqrt{R(\theta)} \cos(2\pi z/\lambda - \phi(\theta)) \quad (5)$$

where $R(\theta)$ is the intensity of the reflected beam and $\phi(\theta)$ is the phase between the incident and reflected beam which varies from π to 0 across the Bragg peak. Eq. (5) can help comparing different X-ray standing wave curves, even in slightly more complex cases. This is illustrated in Fig. 2 where we have represented the calculated fluorescence from a hypothetical 2Å thick layer of ions adsorbed from a 1μm thick film of solution. The fluorescence intensity is rep-

resented for different locations of the surface layer above the interface when this thin layer contains as many ions as the solution (50% of total number of ions), or only 5% of the total number of ions.

Obviously, the sensitivity is very high for the 50% case. However the different location can still be distinguished in a fit with good quality data in the 5% case as the shape of the curve is still significantly different.

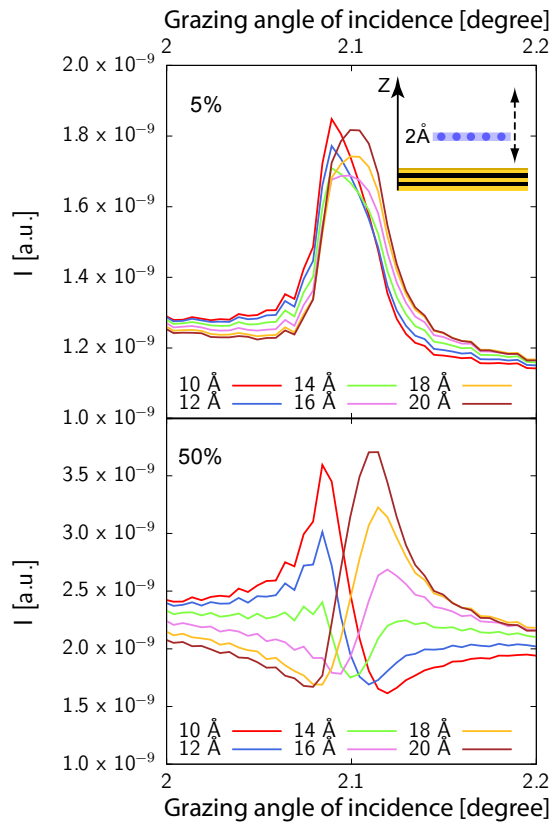


Figure 2: Calculated fluorescence curves for a 2 Å thick layer in a 1 μm liquid film. In the bottom curves, the layer contains as many ions as the rest of the film, and only 5% in the top curves. The layer is positioned at 10 Å, 12 Å, 14 Å, 16 Å, 18 Å and 20 Å above the reference plane. In the experiments, there is a top silica layer in between the reference plane and the layer and the interface is located $\approx 10\text{-}15 \text{ \AA}$ above the reference plane marked by a Cr layer in the experiments.

Experimental methods.

X-ray standing-wave measurements were performed at the DiffAbs beamline of Synchrotron SOLEIL, Saint-Aubin, France. A schematic of the methods used to probe ions at interfaces as well as the setup used at the DiffAbs beamline are shown on Fig. 1. The samples consisted in an ultra thin liquid layer sandwiched between the multilayer substrate used to create the standing waves and a 4 μm thick ultralene® X-ray transparent window (Fig. 1b). The experiments were performed using a 7 keV incident beam energy with a small parallel beam ($250\mu\text{m} \times 200\mu\text{m}$) allowing to resolve the Bragg peaks.

The substrates used in these experiments were Si-W multilayers (150 periods of 2.5 nm) manufactured by AXO (Dresden, Germany). They include a thin ($< 0.5 \text{ nm}$) Cr layer below the top SiO_2 to serve as a reference for the phase. Substrates were cleaned following the RCA cleaning procedure³³ before being used. KCl, CsCl, CsI (Sigma-Aldrich, 99.9995% purity) and KI (Sigma-Aldrich, 99.999% purity) were used without further purification. Molar stock solutions were prepared using water from a Millipore Milli-Q® system (18.2 MΩ.cm resistivity) and further diluted and mixed just before the experiments. Small volumes of solution ranging from 250 nl to 1.5 μl were introduced in the cell. The multilayer was then pressed against the cover ultralene® film allowing for the control of the sample thickness (Fig. 1b). All manipulations were performed in a clean room to avoid dust contamination.

Results

Both reflectivity curves for sample characterization and fluorescence curves around the Bragg peak were recorded for each sample. The full analysis of the results first requires the determination of the liquid layer thickness by X-ray reflectivity. The fluorescence of each ion as a function of the grazing angle of incidence around the Bragg peak (standing wave curve) is then determined by fitting the fluorescence

spectrum for each angle of incidence, and each standing wave curve is finally analysed to obtain the ionic distribution profiles. Bare substrates and empty samples with Ultralene window were first measured as a reference for background subtraction.

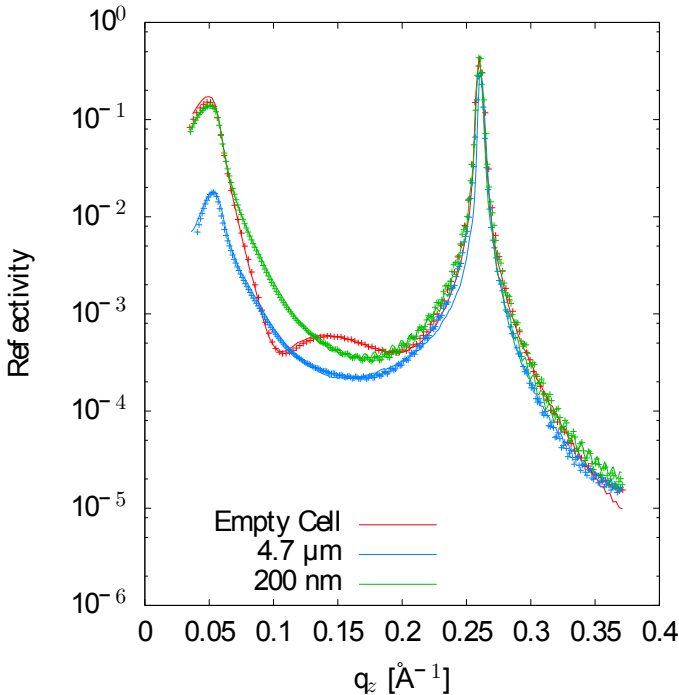


Figure 3: Measured X-ray reflectivity and best fit for an empty cell (no liquid), a $4.7\mu\text{m}$ and a 200nm liquid layer thickness.

Sample thickness determination using X-ray reflectivity.

Reflectivity curves were recorded using a scintillator detector and carefully normalized to the incident beam intensity. They were analyzed using the Reflec software (A.Gibaud, G.Vignaud) based on the matrix method.³¹ We used a model consisting of the multilayer substrate, a solution layer and the $4\mu\text{m}$ thick Ultralene® film which was fitted to the data, allowing to determine the thickness of the liquid layer. Obtaining good fits is important in order to constrain the standing waves analysis. Fig. 3 shows experimental reflectivity curves (as measured, without any corrections) as well as the corresponding fits before and after solu-

tion injection. The fitting procedure includes illuminated area and water layer absorption corrections. In order to determine the thickness from the fit of reflectivity curves, the empty cell curves were fitted first. A solution layer was then added to the model without allowing any change in the multilayer parameters. The change in refractive index when a liquid layer is present modifies the shape of the curve in the $q_z \approx 0.1\text{\AA}^{-1}$ region *i.e.* in between the critical angle for total external reflection at the substrate-solution interface and the Bragg peak (Fig. 3). Though the solution layer is generally either too thick or not homogeneous enough to give rise to fringes that could be resolved in the reflectivity curves, its thickness can nevertheless be determined from the shape of the reflectivity curve in the region below and close to the critical angle ($q_z \sim 0.05\text{\AA}^{-1}$ in Fig. 3). For a very thick layer, the intensity at the critical angle can indeed be reduced by more than one order of magnitude compared to the empty cell because the incident and reflected X-rays will have to travel hundreds of microns in the absorbing solution for grazing angles of incidence in the mrad range, even for a liquid layer thickness $< 1\mu\text{m}$. One should also notice that the thickness we determine is an average over the approximately 8 mm long and $250\mu\text{m}$ wide beam footprint on the sample.

X-ray fluorescence measurements and analysis.

Fluorescence curves were recorded using a 4-element energy sensitive detector and first accurately normalized to the incident beam intensity. The fluorescence curves were analyzed following the procedure detailed in Ref.⁷ using a home made software with a peak model based on the physics of detection, including a Voigtian peak shape, a tail and a shelf.³⁴ The different peak parameters have a simple energy dependence, thus reducing the number of fitting parameters. Another advantage of this method is that the background from photon counting being built up by the shelf contributions, it is automatically and consistently subtracted. In

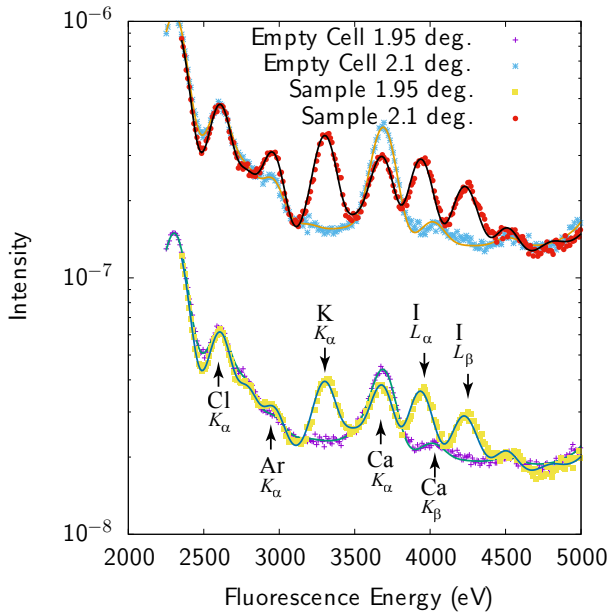


Figure 4: Fluorescence intensity (experiments:symbols - fits:solid lines) recorded at 1.95° and 2.1° (Bragg peak) from an empty cell and a 250nm thick cell filled with a 10mM KCl + 10mM KI solution.

order to determine the interfacial contribution of ions only, we also need to subtract the contribution of elements present in the sample cell, mainly chlorine in the multilayer substrate and calcium in the ultralene film. This is done by manually subtracting the reference sample contribution, yielding standing wave curves for the interface and solution only.

Representative spectra are given on Fig. 4 for a mixture of 10mM solutions of KCl and KI. The Cl K_α line at 2622 eV, the Ar K_α line at 2957 eV (Ar is present in air), the K K_α line at 3313 eV, the Ca K_α and K_β lines at 3690 eV and 4014 eV (Ca is an impurity in the Ultralene film, not affecting the measurements) and the I L_α line at 3938 eV and L_β line at 4220 eV can in particular be identified on Fig. 4. An advantage of fluorescence based methods is their high sensitivity to chemical elements in low quantities (traces). Samples with minute concentration ($10^{-4} M$) or very thin liquid layers (a few 10s of nm) could in particular be studied. Integrated over the beam footprint for a 100nm thick sample, the technique allows to resolve 1 femtomole or better.

The differences in the curves recorded at a grazing angle of incidence of 0.25° below the Bragg peak (1.95°) and at the Bragg peak (grazing angle of incidence of 2.10°) in Fig. 4 directly result from the interfacial distribution of ions. Indeed, shifting the standing wave field distribution, different positions above the interface are probed as shown in Fig. 2. This is however more clearly seen by representing the fluorescence for each chemical element as a function of the grazing angle of incidence around the Bragg peak (standing wave curves).

Standing wave curves.

Typical standing wave curves (fluorescence intensity for each element as a function of the grazing angle of incidence across the Bragg peak) are given on Fig. 5.

Standing wave curves for the thicker sample ($2.85 \mu m$) have a profile which resembles the Bragg peak one. This is expected as these curves are dominated by the homogeneous ionic distribution in the bulk liquid (Fig. 2). Neglecting fluorescence effects close to the interface for a thick solution layer, the fluorescence will be excited by the incident and reflected beam and will be roughly proportional to the incident beam plus reflected beam intensity which is peaked at the Bragg angle. Differences with respect to this shape give access to surface effects which can be determined and are more prominent for thinner samples (like the 250nm thick sample) also shown in Fig. 5. In such a case, the position and the shape of the standing wave curve is already indicative of the position of the ions with respect to the multilayer which is therefore unambiguously determined.

As mentioned above, we analyzed the standing wave curves using a very simple model consisting only of a homogeneous bulk solution and a Stern layer modelled as a stack of 2\AA thick ionic layers, one for each ion. The sample is divided in as many layers as necessary to describe the elemental distribution and the electromagnetic field is calculated in each layer using the matrix method.³¹ Fitting the model (Eq. (5)) to the experimental curve by minimizing the χ^2 function, one obtains the composition, con-

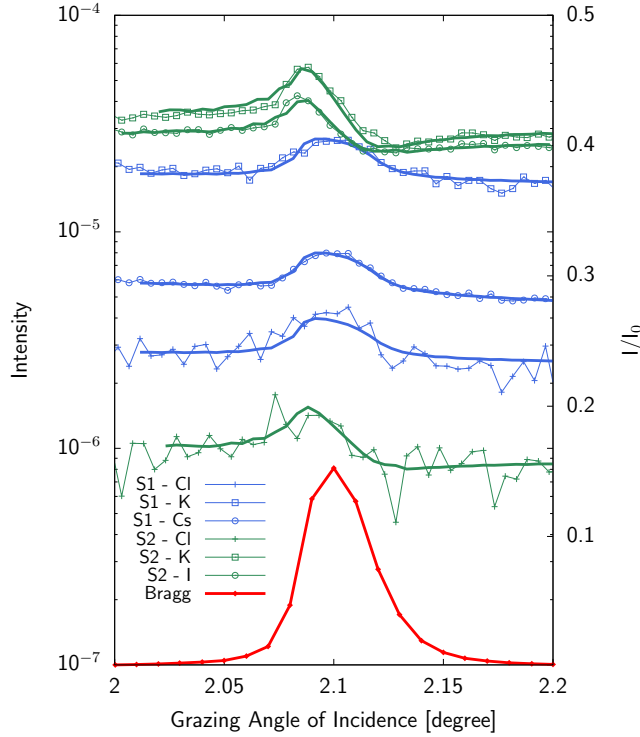


Figure 5: Standing wave curves (experiments:symbols - fits:solid lines) for a mixture of 1mM solutions of KCl and CsCl (S1) and 10mM solutions of KCl and KI (S2). Liquid layer sample thickness was $2.85 \mu\text{m}$ for (S1) and 250nm for (S2) respectively. Curves have been shifted for clarity. The Bragg peak is shown in red as reference. See Table 1 in Supporting Information for fitting parameters.

centration and average position of the different ions in the Stern layer.

In order to get a first check of the consistency of the analysis, we have plotted on Fig. 6 (top) the normalized fluorescence intensity (*i.e.* fluorescence is normalized such as any single ion would give the same fluorescence intensity, this is equivalent to dividing the experimental fluorescence by $B_k T_k$ in Eq. (5)) as a function of the product concentration times thickness, which gives the expected number of ions in the cell. As can be seen in Fig. 6 (top), there is good correlation between fluorescence intensity and the expected number of ions: in other words fluorescence nicely follows the total number of ions. This result shows that both the fluorescence measurements, including the background subtraction procedure for chloride, and thick-

ness determination using reflectivity curves give consistent results.

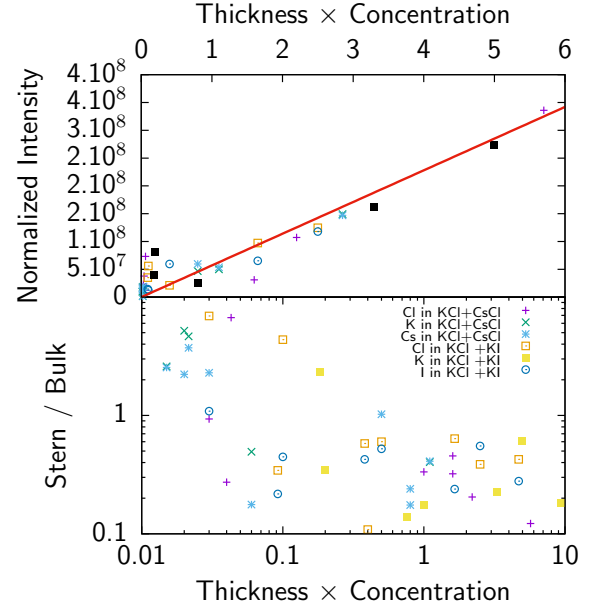


Figure 6: Top: Normalized fluorescence of all ions as a function of the sample thickness times solution concentration. Bottom: Ratio of the number of ions in the Stern layer to the number of ions in the bulk as a function of product thickness \times concentration.

Discussion

Gouy-Chapman-Stern model.

The simplest model used to calculate the distribution of ions at interfaces is the Gouy-Chapman-Stern model.^{1,35} The electric potential ϕ in the double layer obeys the Poisson equation:

$$\frac{d^2\phi}{dz^2} = -\frac{\rho}{\epsilon_0\epsilon_r}. \quad (6)$$

In Eq. (6), $\rho = \sum_i n_i e z_i$ is the charge density, with n_i the concentration of the ion i of valency z_i . $e = 1.602 \times 10^{-19}\text{C}$ is the elementary charge, $\epsilon_0 = 8.85 \times 10^{-12}\text{F/m}$ is the vacuum permittivity and ϵ_r the relative permittivity. Concentrations in the double layer obey a Boltzmann distribution:

$$n_i = n_{i\infty} \exp\left(-\frac{z_i e \phi}{k_B T}\right), \quad (7)$$

with k_B the Boltzmann constant and T the temperature. Insertion of Eq.(7) into Eq.(6) gives after simple integration the Poisson-Boltzmann equation for the potential:

$$\left(\frac{d\phi}{dz}\right)^2 = \frac{2k_B T}{\epsilon_0 \epsilon_r} \sum_i n_{i\infty} \left[\exp\left(-\frac{z_i e \phi}{k_B T}\right) - 1 \right]. \quad (8)$$

The charge in the double layer can be written:

$$\sigma_{DL} = \int_d^\infty \rho(z) dz = - \int_d^\infty \epsilon_0 \epsilon_r \frac{d^2 \phi}{dz^2} = -\epsilon_0 \epsilon_r \left. \frac{d\phi}{dz} \right|_d^\infty, \quad (9)$$

where d is the location of the “outer Helmholtz plane” which fixes the border between the Stern layer and the diffuse layer (Fig. 7).

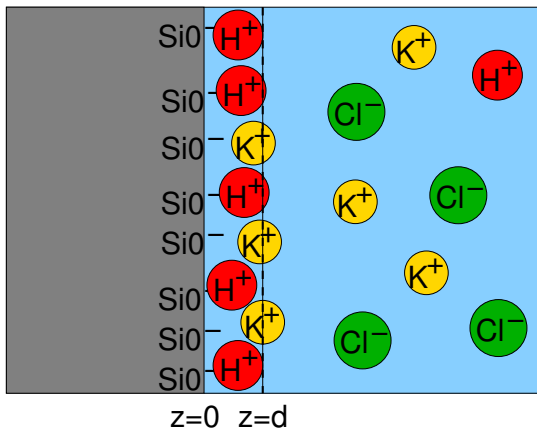


Figure 7: Schematics of the Stern layer and the double layer. $z=d$ is the location of the outer Helmholtz plane.

By inserting Eq. (8) in Eq. (9), one obtains.

$$\sigma_{DL}^2 = 2k_B T \epsilon_0 \epsilon_r \sum_i z_i n_{i\infty} \left[\exp\left(-\frac{z_i e \phi(d)}{k_B T}\right) - 1 \right], \quad (10)$$

known as the Grahame equation, which relates the charge in the electric double layer σ_{DL}^2 to the potential at the outer Helmholtz plane $\phi(d)$. On the other hand, the composition of the Stern layer is determined by surface equilibria, related to the dissociation of surface silanol groups for our silica surface. For protons and a monova-

lent salt with cation Me^+ , one would have:

$$\begin{aligned} \Gamma_{SiO^-}[H^+]_{z=0} &= \Gamma_{SiO^-}[H^+] \exp\left(-\frac{e\phi(0)}{k_B T}\right) \\ &= K_H \Gamma_{SiOH}, \end{aligned} \quad (11)$$

and

$$\begin{aligned} \Gamma_{SiO^-}[Me^+]_{z=d} &= \Gamma_{SiO^-}[Me^+] \exp\left(-\frac{e\phi(d)}{k_B T}\right) \\ &= K_{Me^+} \Gamma_{SiOC}, \end{aligned} \quad (12)$$

where the concentrations involving silanol groups Γ_{SiOH} , Γ_{SiO^-} and Γ_{SiOC} are surface concentrations and it has been made explicit that H^+ ions are located at height 0 and Me^+ cations at height d . K_H and K_{Me^+} are equilibrium constants. The total density of surface sites is

$$\Gamma = \Gamma_{SiO^-} + \Gamma_{SiOH} + \Gamma_{SiOC}. \quad (13)$$

The potential dependence in the Stern layer can be obtained by considering the Stern layer as a molecular condenser of capacitance C_{Stern} where the potential drop is linear:

$$\phi(d) - \phi(0) = \sigma_0 / C_{Stern}. \quad (14)$$

We now have a full set of equations Eqs. (10)-(14) which can be solved numerically to determine all surface and bulk concentrations.

A bare surface density of sites $\Gamma = 8 \text{ SiO}^-$ sites $/\text{nm}^2$ (reduced by protonation and ion complexation, Eq. (13)), a capacitance of the Stern layer $C_{Stern} \approx 2.9 \text{ F/m}^2$ and $K_H = 10^{-7.5} - 10^{-7}$ are well established in the literature.³⁶ The complexation constants for cations are less documented. Davis et al.³⁷ report a much weaker specific adsorption for SiO_2 than for the other oxides, with $pK_K \approx 0.5$. Sonnefeld³⁸ suggests an even weaker binding. On the contrary, Tao et al.³⁹ and Zhao et al.²⁴ give $pK_K = 1$ and $pK_K = 2$ respectively, and the results of Dishon et al.²² are consistent with even larger values (see Fig. 8 bottom).

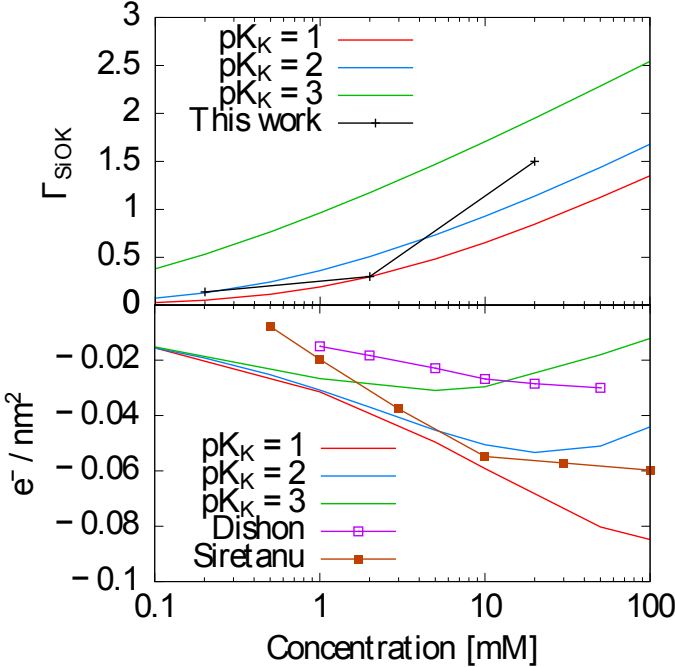


Figure 8: Top: Γ_{SiOK} as measured in this work and calculated using the Gouy-Chapman-Stern model as explained above with $pK_K=2$. Bottom: Surface charge calculated using the same model with $pK_K=1,2$ and 3 together with measurements from Dishon et al.²² and Siretanu et al.,²³ showing the consistency with our results.

Partition between Stern layer and solution.

In contrast to the previous estimates of pK_K , our measurements provide a direct access to surface concentrations. We find Potassium surface concentrations in the Stern layer of $0.14/nm^2$, $0.3/nm^2$ and $1.5/nm^2$ for $0.1mM$, $1mM$ and $10mM$ KCl / KI mixtures respectively. As an indication, a $1/nm^2$ surface concentration would correspond for a 2\AA thick layer to a concentration of 3mol/l .

These results can be compared to the Gouy-Chapman-Stern model presented above in order to check whether they are in the expected range. With $pK_K = 2$, we obtain $\Gamma_{SiOK} \approx 0.13/nm^2$ for a $0.1mM$ solution of KCl at pH=7, $\Gamma_{SiOK} \approx 0.5/nm^2$ for a $1mM$ solution and $\Gamma_{SiOK} \approx 1.13/nm^2$ for a $10mM$ solution, in fairly good agreement with our experimental results (Fig. 8 (top)). As shown on Fig. 8 (top), the agreement is less good with $pK_K=1$ for the

$10mM$ solution and significantly less good for all concentrations with $pK_K=3$.

Previous experiments gave access to the effective surface charge Γ_{SiO^-} instead of the K^+ concentration in the Stern layer. Using the Gouy-Chapman-Stern model, we can calculate Γ_{SiO^-} using the same parameters for different concentrations, allowing for an indirect comparison of our results to previous experiments^{22,23}. Note that in both Refs.²² and,²³ surfaces were prepared by plasma cleaning which might lead to a different surface chemistry. Whereas Ref.²² shows a better agreement with $pK_K=3$ Ref.,²³ shows better agreement with $pK_K=2$ as in our case.

A difference between the model and our measurements is that there is a finite reservoir of ions in our experiments, in contrast with the theory which assumes a fixed concentration. Using the Gouy-Chapman-Stern model, one expects to have in between $\approx 0.4 \times 10^{14}$ and $\approx 6 \times 10^{14}$ ions in the Stern layer on a $2 \times 2cm^2$ substrate (for $\Gamma_{SiOK} \approx 0.1/nm^2$ and $\Gamma_{SiOK} \approx 1.5/nm^2$ respectively).

We typically spread $500\text{nl} - 1\ \mu\text{l}$ droplets containing $3 - 6 \times 10^{14}$ ions for a mM solution. This crude calculation shows that a range of 0.1 to 10 is expected for the surface to bulk concentration ratio. The ratio of adsorbed ions in the Stern layer with respect to the total number of ions in the bulk is represented on Fig. 6 (bottom). This ratio ranges from 0.1 for thick and concentrated samples to ≈ 5 for thin layers and dilute solutions where a significant amount of ions go to the surface in agreement with the previous estimate. It also implies that the above modeling using the Poisson-Boltzmann-Stern approach, which requires an infinite reservoir, cannot be used without caution, at least for the least concentrated solutions ($0.1mM$).

A ratio of 0.1 to 10 falls well in the range where the different elements can be located as discussed earlier and explains why some curves are “bulk-like” with standing wave curves having a shape which resembles the Bragg peak (concentrated thick samples) and why “surface-like” features are more prominent in others.

It should be noted here that as the Stern layer is much thinner and concentrated than the total

film, the standing wave curve is mainly sensitive to the Stern layer and it is more difficult to determine a concentration profile in the rest of the film.

Distribution within the Stern layer.

The standing wave technique also allows for the determination of the position of ions relative to the multilayer lattice, and therefore relative to each other. Most interesting is of course the competition between K^+ and Cs^+ in KCl and CsCl mixtures and between Cl^- and I^- in KCl and KI mixtures.

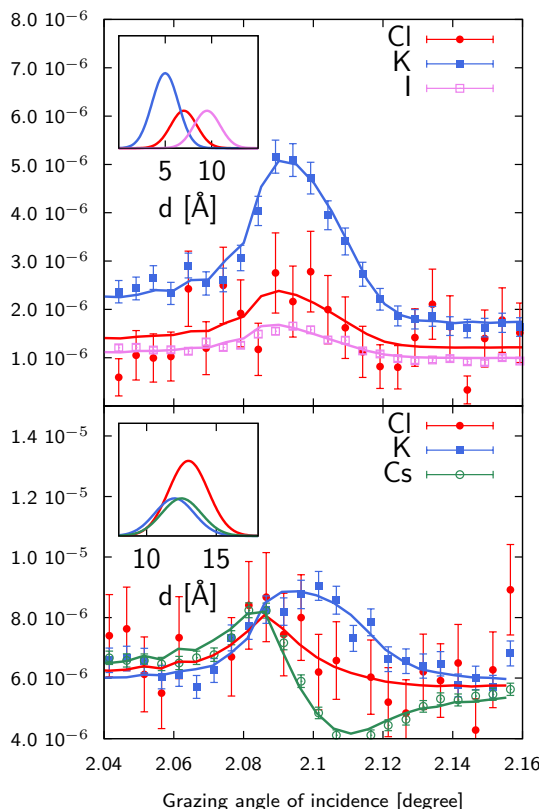


Figure 9: X-ray standing wave curves and ionic distributions (insets) for a 1mM KCl/CsCl mixture (bottom) and a 1mM KCl/KI mixture (top). The KCl/CsCl sample was 50nm thick and the KCl/KI sample was 120nm thick sample. The width of the distributions has been set equal to the surface roughness. As we do not determine absolute concentrations, the distributions have been scaled arbitrarily. See Table 1 in Supporting Information for fitting parameters.

Two representative examples are given on Fig. 9 for a 1mM KCl/CsCl mixture in a 50nm thick sample and a 1mM KCl/KI mixture in a 120nm thick sample. The XSW curves have been analysed using the model described above, where the ionic distributions have been convolved with the surface roughness. We first note that there is a large concentration of both cations and anions in a 4 to 5 Å thick layer, with concentrations ≈ 100 times larger than in the bulk of the film. Then, looking more deeply into the details, we see that in all cases, cations are located closer to the surface than anions, as expected for a negatively charged surface, and K^+ and Cs^+ show an almost equal propensity for the surface. Regarding the competition between Cl^- and I^- , we find that the center of the Cl^- distribution is systematically closer to the surface, compared to the I^- distribution. In this case the shift is 2.5Å (see top insert of Fig.9). This is in contrast with the air-water interface where I^- was shown to have a higher propensity for the surface compared to Cl^- .⁷ Interestingly enough, this higher propensity of the Cl^- ions for the surface is also reflected in the Stern layer concentration as we find a $\approx 1.6 \pm 0.3$ larger concentration of chloride ions compared to iodide ions. These two findings are not necessarily in contradiction since both the surface chemistry (affecting short range interactions), including interaction with the other ions, and the dielectric function (affecting the dispersion forces) are different.

Conclusion

In this paper, we have shown that X-ray standing waves can be used to investigate ionic distributions in nanometer thick liquid layers using surfaces and ions of broad interest in colloidal science and nanoscience. Not only the amount of ions in the bulk and Stern layer can be determined, but also their distribution in the direction perpendicular to the surface. Confronting such data to simulations taking into account all molecular interactions^{40,41} should lead to a detailed understanding of ionic distributions at aqueous interfaces which is of utmost impor-

tance for several areas of science.

Acknowledgements: The authors gratefully thank Christian Blot for manufacturing the sample cell and Elodie Barret for concentration measurements of the solutions using capillary electrophoresis. The Marie Skłodowska Curie initial Training network SOMATAI under EU Grant Agreement No. 316866 is gratefully acknowledged for funding the PhD grant of Soumaya ben Jabrallah.

References

1. Lyklema, J. Fundamentals of Interface and Colloid Science Volume 2, Solid-Liquid Interfaces; Academic Press, 1995.
2. Collins, K.; Washabaugh, M. The Hofmeister effect and the behaviour of water at interfaces. Quarterly Reviews of Biophysics **1985**, 18, 323–422.
3. Cacace, M.; Landau, E.; Ramsden, J. The Hofmeister series: salt and solvent effects on interfacial phenomena. Quarterly Reviews of Biophysics **1997**, 30, 241–277.
4. Kunz Ed., W. Specific Ion effects; World Scientific: Singapore, 2009.
5. Jungwirth, P.; Tobias, D. Specific ion effects at the air/water interface. Chemical Reviews **2006**, 106, 1259–1281.
6. Koelsch, P.; Viswanath, P.; Motschmann, H.; Shapovalov, V. L.; Brezesinski, G.; Mohwald, H.; Horinek, D.; Netz, R. R.; Giewekemeyer, K.; Alditt, T. S. et al. Specific ion effects in physicochemical and biological systems: Simulations, theory and experiments. Colloids Surfaces A-physicochemical Engineering Aspects **2007**, 303, 110–136.
7. Padmanabhan, V.; Daillant, J.; Belloni, L.; Mora, S.; Alba, M.; Konovalov, O. Specific ion adsorption and short-range interactions at the air aqueous solution interface. Phys. Rev. Lett. **2007**, 99.
8. Koopal, L.; Saito, T.; Pinheiro, J.; van Riemsdijk, W. Ion binding to natural organic matter: General considerations and the NICA-Donnan model. Colloids and Surfaces A **2005**, 265, 40–54.
9. Bocquet, L.; Charlaix, E. Nanofluidics, from bulk to interfaces. Chemical Society Reviews **2010**, 39, 1073–1095.
10. Pu, Q.; Yun, J.; Temkin, H.; Liu, S. Ion-enrichment and ion-depletion effect of nanochannel structures. Nanoletters **2004**, 4, 1099–1103.
11. Stein, D.; Kruithof, M.; Dekker, C. Surface-Charge-Governed Ion Transport in Nanofluidic Channels. Phys. Rev. Lett. **2004**, 93, 035901.
12. Karnik, R.; Fan, R.; Yue, M.; Li, D.; Yang, P.; Majumdar, A. Electrostatic control of ions and molecules in nanofluidic transistors. Nanoletters **2005**, 5, 943–948.
13. Huang, D.-M.; Cottin-Bizonne, C.; Ybert, C.; Bocquet, L. Ion-Specific Anomalous Electrokinetic Effects in Hydrophobic Nanochannels. Physical Review Letters **2007**, 98, 177801.
14. Weber, R.; Winter, B.; Schmidt, P.; Widdra, W.; Hertel, I.; Dittmar, M.; Faubel, M. Photoemission from Aqueous Alkali-Metal-Iodide Salt Solutions Using EUV Synchrotron Radiation. Journal of Physical Chemistry B **2004**, 108, 4729–4736.
15. Cheng, M.; Callahan, K.; Margarella, A.; Tobias, D.; Hemminger, J.; Bluhm, H.; Krisch, M. Ambient Pressure X-ray Photoelectron Spectroscopy and Molecular Dynamics Simulation Studies of Liquid/Vapor Interfaces of Aqueous NaCl, RbCl, and RbBr Solutions. Journal of Physical Chemistry C **2012**, 116, 4545–4555.
16. Brown, M.; Abbas, Z.; Kleibert, A.; Green, R.; Goel, A.; May, S.; Squires, T. Determination of Surface Potential and Electrical Double-Layer Structure at the

- Aqueous Electrolyte-Nanoparticle Interface. *Physical Review X* **2016**, 6, 011007.
17. Brown, M.; Goel, A.; Abbas, Z. Effect of Electrolyte Concentration on the Stern Layer Thickness at a Charged Interface. *Angew. Chem. Int. Ed* **2016**, 55, 3790–3794.
18. Raymond, E.; Richmond, G. Probing the Molecular Structure and Bonding of the Surface of Aqueous Salt Solutions. *Journal of Physical Chemistry B* **2004**, 108, 5051–5059.
19. Gopalakrishnan, S.; Liu, D.; Allen, H.; Kuo, M.; Shultz, M. Vibrational Spectroscopic Studies of Aqueous Interfaces: Salts, Acids, Bases, and Nanodrops. *Chemical Reviews* **2006**, 106, 1155–1175.
20. Sloutskin, E.; Baumert, J.; Ocko, B.; Kuzmenko, I.; Checco, A.; Tamam, L.; Ofer, T., E. Gog; Gang, O.; Deutsch, M. The surface structure of concentrated aqueous salt solutions. *Journal of Chemical Physics* **2007**, 126, 054704.
21. Duval, J.; Bera, S.; Michot, L.; Daillant, J.; Belloni, L.; Konovalov, O.; Pontoni, D. X-Ray Reflectivity at Polarized Liquid-Hg-Aqueous-Electrolyte Interface: Challenging Macroscopic Approaches for Ion-Specificity Issues. *Physical Review Letters* **2012**, 108.
22. Dishon, M.; Zohar, ; Sivan, U. From Repulsion to Attraction and Back to Repulsion: The Effect of NaCl, KCl, and CsCl on the Force between Silica Surfaces in Aqueous Solution. *Langmuir* **2009**, 25, 2831–2836.
23. Siretanu, I.; Ebeling, D.; Andersson, M.; Stipp, S.; Philipse, A.; Cohen Stuart, M.; van den Ende, D.; Mugele, F. Direct observation of ionic structure at solid-liquid interfaces: a deep look into the Stern Layer. *Scientific Reports* **2014**, 4.
24. Zhao, C.; Ebeling, D.; Siretanu, I.; van der Ende, D.; Mugele, F. Extracting local surface charges and charge regulation behavior from atomic force microscopy measurements at heterogeneous solid-electrolyte interfaces. *Nanoscale* **2015**, DOI:10.1039/c5nr05261k.
25. Zegenhagen, J. Surface structure determination with X-ray standing waves. *Surface Science Reports* **1993**, 18, 202–271.
26. Schneck, E.; Demé, B. Structural Characterization of Soft Interfaces by Standing-Wave Fluorescence with X-Rays and Neutrons. *Current Opinion in Colloid and Interface Science* **2015**,
27. Bedzyk, M.; Bommarito, G.; Caffrey, M.; Penner, T. Diffuse-Double Layer at a Membrane-Aqueous Interface Measured with X-ray Standing Waves. *Science* **1990**, 248, 52–56.
28. Park, C.; Fenter, P.; Nagy, K.; Sturchio, N. Hydration and Distribution of Ions at the Mica-Water Interface. *Physical Review Letters* **2006**, 97, 016101.
29. Zegenhagen, J., Ed. *The X-Ray Standing Wave Technique: Principles and Applications*; World Scientific Publishing, 2013.
30. Bedzyk, M. J.; Bilderback, D.; White, J.; Abruna, H. D.; Bommarito, M. G. Probing electrochemical interfaces with x-ray standing waves. *The Journal of Physical Chemistry* **1986**, 90, 4926–4928.
31. Gibaud, A.; Vignaud, G. Specular reflectivity from smooth and rough surfaces. X-ray and neutron reflectivity: principles and applications. Berlin Heidelberg, 2009; pp 87–139.
- 32.
33. Kern, W. The Evolution of Silicon Wafer Cleaning Technology. *J. Electrochem. Soc.*, **1990**, 137, 1887–1892.
34. van Gysel, M.; Lemberge, P.; van Espen, P. Implementation of a spectrum fitting procedure using a robust peak model. *X-ray Spectrometry* **2003**, 32, 434–441.

35. Trefalt, G.; Behrens, S.; Borkovec, M. Charge Regulation in the Electrical Double Layer: Ion Adsorption and Surface Interactions. *Langmuir* **2015**, 32, 380–400.
36. Hiemstra, T.; de Wit, J.; van Riemsdijk, W. Multisite Proton Adsorption Modeling at the Solid/Solution Interface of (Hydr)oxides: A New Approach II. Application to Various Important (Hydr)oxides. *Journal of Colloid and Interface Science* **1989**, 133, 105–117.
37. Davis, J.; James, R.; Leckie, J. Surface Ionization and Complexation at the Oxide/Water Interface I. Computation of Electrical Double Layer Properties in Simple Electrolytes. *Journal of Colloid and Interface Sctence* **1978**, 63, 480–499.
38. Sonnfeld, J. Surface charge density on spherical silica particles in aqueous alkali chloride solutions Part 2. Evaluation of the surface charge density constants. *Colloid and Polymer Science* **1995**, 273, 932–938.
39. Tao, Z.; Zhang, H. Acidity and Alkali Mrtal Adsorption on the SiO₂ - Aqueous Solution Interface. *Journal of Colloid and Interface Science* **2002**, 252, 15–20.
40. Schwierz, N.; Horinek, D.; Netz, R. Anionic and Cationic Hofmeister Effects on Hydrophobic and Hydrophilic Surfaces. *Langmuir* **2013**, 29, 2602–2614.
41. Schwierz, N.; Horinek, D.; Netz, R. Specific Ion Binding to Carboxylic Surface Groups and the pH Dependence of the Hofmeister Series. *Langmuir* **2015**, 31, 215–225.